

Simulation of the Taylor–Green Vortex Using High-Order Flux Reconstruction Schemes

J. R. Bull* and A. Jameson†
Stanford University, Stanford, California 94305

DOI: 10.2514/1.J053766

In this paper, the ability of high-order flux reconstruction numerical schemes to perform accurate and stable computations of compressible turbulent flows on coarse meshes is investigated. Two new flux reconstruction schemes, which are optimized for wave dissipation and dispersion properties, are compared to the nodal discontinuous Galerkin and spectral difference methods recovered via the energy-stable flux reconstruction method. The Taylor–Green vortex benchmark problem at $Re = 1600$ is used as a simple a priori test of the numerics. Dissipation rates computed from kinetic energy, vorticity, and pressure dilatation are plotted against reference solutions. Results show that, at low mesh resolution, the flux reconstruction schemes are highly accurate across a range of orders of accuracy, although oscillations can appear in the solution at orders of six and above. Although the flux reconstruction method has a built-in stabilization mechanism, an additional means of damping these instabilities is required. The schemes vary in the amount of numerical dissipation and resolution of the turbulent spectrum. One of the optimized flux reconstruction schemes (the optimized flux reconstruction scheme) is shown to have greater spectral accuracy than any of the others tested, motivating its future usage for high-order high-fidelity computational fluid dynamics.

Nomenclature

c	=	free parameter in flux reconstruction method
E_k	=	kinetic energy
e	=	energy
f	=	flux vector
g_L, g_R	=	left and right correction functions
J	=	Jacobian
k	=	wave number
L_p	=	degree p Legendre polynomial
l_i	=	i th Lagrange polynomial
N	=	number of solution points per direction per element
p	=	pressure
p	=	polynomial order
S	=	rate of strain tensor
u	=	solution vector
u, v, w	=	velocity components
ϵ_1	=	energy-based dissipation rate
ϵ_2	=	vorticity-based dissipation rate
ϵ_3	=	strain-based dissipation rate
ϵ_4	=	bulk viscosity-based dissipation rate
ϵ_5	=	dilatation-based dissipation rate
ζ	=	enstrophy
ξ	=	local coordinate
ρ	=	density
Ω	=	domain
ω	=	vorticity

I. Introduction

THE well-established computational fluid dynamics (CFD) techniques of second-order numerical schemes and Reynolds-averaged Navier–Stokes (RANS) turbulence models are capable of

predicting steady attached flows at cruise conditions, but they are incapable of predicting conditions at the fringes of the flight envelope, which are often characterized by turbulent separated flows [1]. Many other aerodynamic problems of central importance also feature complex turbulent flows, including combustion, acoustic noise prediction, and the design of hypersonic vehicles. To improve the performance, efficiency, and safety of future generations of aircraft, CFD must move beyond the current plateau of second-order RANS methods and establish a new norm of high-order-accurate high-fidelity simulation.

High-order-accurate ($p > 1$) numerical methods offer significantly better wave and vortex propagation properties than second-order-accurate ($p = 1$) schemes, thanks in large part to their lower numerical dissipation. The development of high-order-accurate finite difference schemes brought about new levels of accuracy in aeroacoustic problems [2]; however, the extension to unstructured meshes remains a major roadblock to their use for flows over and through complex geometry. Over the past two decades, discontinuous Galerkin (DG) methods have proved to be highly successful for high-order-accurate simulations in complex geometry, owing to their formulation on full hybrid meshes [3,4]. Classical DG methods construct integral operators over element volumes and surfaces by integrating the equations by parts, and they represent the solution within each element as a modal expansion of locally orthogonal polynomials [5]. This has the advantages of making the mass matrix diagonal and enabling exact evaluation of the integrals, but classical DG can be expensive if standard Gaussian quadrature rules are employed [6]. Nodal DG (NDG) methods, in contrast, represent the solution as nodal values at a set of interpolation points [7]. By relinquishing exact integration, NDG methods are computationally cheaper but tend to require additional stabilization [6,7]. The DG spectral element method (DGSEM) represents the solution in classical form but performs integration cheaply using cheap quadrature formulas [8,9]. Gassner et al. [10] devised efficient quadrature schemes for arbitrarily shaped elements based on the nodal DG approach.

Recently, the collocation-based NDG method has been recast in differential form as the spectral difference (SD) [11,12] and the flux reconstruction (FR) methods [13]. Flux reconstruction is a general high-order framework that, in the case of linear fluxes, recovers particular collocation-based NDG and SD methods, as well as allowing for the definition of new schemes [13]. The FR framework is easy to implement on unstructured meshes, allows for tuning of the numerical properties, and is cheap to compute owing to the lack of integration procedures. A family of energy-stable flux reconstruction (ESFR) schemes have been developed by the Aerospace Computing Laboratory (ACL) at Stanford University [14]. The ESFR schemes

Presented as Paper 2014-3210 at the 7th AIAA Theoretical Fluid Mechanics Conference, Atlanta, GA, 16–20 June 2014; received 29 July 2014; revision received 27 March 2015; accepted for publication 19 May 2015; published online 30 July 2015. Copyright © 2015 by the American Institute of Aeronautics and Astronautics, Inc. All rights reserved. Copies of this paper may be made for personal or internal use, on condition that the copier pay the \$10.00 per-copy fee to the Copyright Clearance Center, Inc., 222 Rosewood Drive, Danvers, MA 01923; include the code 1533-385X/15 and \$10.00 in correspondence with the CCC.

*Postdoctoral Scholar, Dept. of Aeronautics and Astronautics. Member AIAA.

†Thomas V. Jones Professor, Dept. of Aeronautics and Astronautics. Fellow AIAA.

were proven to be stable in an energy norm of Sobolev type for the one-dimensional (1-D) linear advection equation for all orders of accuracy on an arbitrary mesh [14]. Hence, the ESFR schemes can be formulated on quadrilateral and hexahedral elements by taking tensor products of 1-D operators. Subsequently, the stability proof was extended to the linear advection-diffusion equation in 1-D [15], on triangles [16], and on tetrahedra [17]. The energy norm contains a nonnegative coefficient c that allows for the recovery of particular collocation-based NDG (with $c = 0$) and SD ($c = c_{SD}$) schemes (henceforth denoted as FR-NDG and FR-SD, respectively), as well as the G_2 scheme ($c = c_{G2}$) of Huynh [13] and an infinite variety of new stable schemes [14].

For nonlinear fluxes, high-order methods are well known to be susceptible to aliasing instabilities caused by inexact representation of the true flux in a finite-dimensional polynomial subspace [7]. The aliasing error associated with the ESFR schemes arises from the use a collocation projection of the flux at the solution points [18]. It was shown for the ESFR schemes in 1-D that the error is minimized by choosing the solution points to be the Gaussian quadrature points [18]. Recently, enhanced nonlinear stability has also been achieved in simplex elements by devising new quadrature schemes [19]. Even so, the aliasing error is still present and can become significant at higher orders of approximation, so some additional control over aliasing errors is sought. High-fidelity turbulent flow simulations, which do not resolve the entire range of motions, also incur a closure error (well known in the field of large-eddy simulation) due to the lack of dissipation of the resolved scales by the subgrid scales. The development of methods to deal with this ‘‘closure problem’’ in the context of high-order schemes is a vigorous area of research that shares much common ground with stabilization techniques.

Many techniques have been proposed for controlling aliasing and closure errors in high-order numerical methods. A stabilization technique developed specifically for high-order methods is to apply a low-pass filter to the polynomial basis in order to reduce or remove destabilizing high wave number components [9,20,21]. An equivalent approach is to include a high-order derivative term: for example, the spectral vanishing viscosity (SVV) method [22,23]. SVV and low-pass filtering can also be used to address the closure problem, i.e., by introducing artificial dissipation to represent the effect of the subgrid scales [20,24–28]. A technique intended solely for stabilization of high-order schemes is overintegration, which is also known as polynomial dealiasing, but this incurs a high computational cost [9,29]. Perhaps the simplest stabilization method, commonly used with second-order schemes, is upwinding of the interface fluxes: for example, by Roe’s method [30]. Upwinding with a Roe flux was shown to improve the stability of the ESFR schemes (compared to central flux) in 1-D by Vincent et al. [14]. It was shown by Jameson and Lodato [31] that, for the ESFR schemes, the amount of dissipation added by the interface flux is proportional to a high-order derivative of the solution, thus providing an efficient damping of the energy in the high-order modes. The coefficient c in the ESFR schemes offers another means of control over stability. Setting $c > 0$ was shown to have a stabilizing effect compared to the baseline case of $c = 0$ by Vincent et al. [14]. However, accuracy was reduced at the same time, implying that the choice of c is a compromise between stability and accuracy. It was shown by Allaneau and Jameson [32] that a nonzero value of c is identical to applying a low-pass filter to the residual in the case of a linear flux. With all of these techniques, it is vital to maintain the advantage of using high-order methods over second-order methods by only adding enough dissipation to stabilize the scheme, but not so much that the propagation of turbulence and other wave phenomena is adversely affected.

Investigation of the spectral properties of FR schemes provides an insight into their ability to resolve multiscale phenomena such as turbulence. Vincent et al. [33] carried out a von Neumann analysis of the ESFR schemes, finding that the FR-SD method had the lowest dispersion error [they also identified a value of c that maximized the allowable Courant–Friedrichs–Lewy (CFL) condition]. Recently, Asthana and Jameson [34] conducted a full modal analysis of the FR method in 1-D to obtain dissipation and dispersion relations for each mode. They solved an optimization problem to identify a value of c in

the ESFR schemes that minimized errors associated with wave dissipation and dispersion; the optimized scheme is henceforth referred to as the optimized ESFR (OESFR) scheme. They went further to carry out a multidimensional constrained optimization of the general FR method, identifying a scheme outside the ESFR family that is optimal in terms of wave propagation, henceforth referred to as the optimized FR (OFR) scheme. We hypothesize that, by virtue of their superior resolution of the energy-containing modes, these optimized schemes will be more accurate than other FR schemes. It is shown here that the benefits of the optimized schemes will be carried to higher dimensions by taking tensor products. However, with superior accuracy comes inferior stability: the optimized schemes are more susceptible to aliasing-driven instabilities. Control over aliasing errors in FR schemes is a topic of current research within the ACL.

In this paper, we analyze the behavior of the flux reconstruction method in underresolved compressible turbulent flow. The Taylor–Green vortex (TGV) benchmark problem at $Re = 1600$ is an ideal test case due to the deterministic nature of the flow, yet it contains many of the features of real turbulent flows, including vortex stretching and interaction, as well as dilatation (compressibility) effects. It has been used by many authors for high-order method validation, including Beck and Gassner [9], Diosady and Murman [29], Chapelier et al. [5], Don et al. [35], Johnsen et al. [36] and Carton de Wiart et al. [37]. The TGV was identified as a challenging problem for high-order methods in the first, second and third international workshops on high-order CFD methods. Bull and Jameson [38] simulated the TGV problem with the FR-SD scheme, matching high-resolution reference data on relatively coarse hexahedral and tetrahedral grids. Results using more schemes and polynomial orders are presented in this paper, and new details of the ability of the FR schemes to represent compressible turbulent flows emerge. The simulations are carried out using HiFiLES, the ACL’s open-source unstructured graphical processing unit (GPU)-accelerated flux reconstruction solver. Details of the code and its verification and validation can be found in work by Lopez et al. [39].

It is shown that the FR method accurately predicts the mean turbulent energy cascade and the important flow structures on relatively coarse grids, thanks to the high order of accuracy and to low dissipative and dispersive errors. The stabilization provided by the FR method sufficiently damps instabilities at polynomial orders of five or less, with the amount of damping depending on the particular scheme. At higher than the fifth order, all schemes display instabilities at low mesh resolution (sometimes leading to residual divergence), which requires further stabilization: for example, in the form of a filter. Current work at the ACL is directed at this important topic. The OESFR scheme developed by Asthana and Jameson [34] displays nearly identical behavior to the FR-NDG scheme. The OFR scheme [34] is as stable as, but more accurate than, the FR-SD and FR-NDG schemes. Energy spectra show that the OFR scheme provides superior resolution of the energy in the higher wave numbers, confirming that the analysis of Asthana and Jameson [34] is applicable to the Navier–Stokes equations in three dimensions.

These results lend support to the further use of high-order FR schemes (and, in particular, the newly developed OFR scheme) for large-eddy simulation (LES) of high-Reynolds-number turbulent flows. Their turbulence-resolving abilities and low numerical dissipation make them suitable for applications involving far-field propagation of vortices and waves, including aircraft noise prediction and boundary layer ingestion. Future work will include the development of de-aliasing filters to improve stability at higher orders and investigation of the suitability of the OFR scheme for more complex high-Reynolds-number turbulent flows.

II. High-Order Flux Reconstruction

A. General Formulation

The compressible Navier–Stokes equations are discretized using the high-order flux reconstruction scheme. We write the equations in conservative form in a three-dimensional (3-D) domain Ω with spatial coordinates $\mathbf{x} = \{x_1, x_2, x_3\}$ and time t :



Fig. 1 Solution and flux points (circles) and interface flux points (squares) in 1-D for $p = 2$.

$$\frac{\partial \mathbf{u}}{\partial t} + \frac{\partial \mathbf{f}}{\partial x} = 0 \quad (1)$$

where $\mathbf{u} = (\rho \ \rho u \ \rho v \ \rho w \ \rho e)^T$ are the conservative variables, and \mathbf{f} is the flux. The domain is split into nonoverlapping elements Ω_j . For simplicity, we consider the one-dimensional case. Inside the element, a degree p polynomial, defined on a set of $N = p + 1$ points, is used to represent the solution and the flux, resulting in an N th-order-accurate scheme. The Gauss–Legendre quadrature points (shown with circles in Fig. 1) are chosen, as they were found to minimize aliasing errors for nonlinear problems [18]. Additionally, fluxes are defined at the element interfaces (shown as squares in Fig. 1) to facilitate coupling to neighboring elements.

The piecewise-continuous p th-order solution polynomial $u(x)$ is defined as

$$u(x) = \sum_{i=1}^N u_i l_i(x) \quad (2)$$

where $u_i(x)$ are the nodal solution values at the solution points, and $l_i(x)$ is a set of basis functions: in this case, the Lagrange polynomials. A similar expression is used to obtain the p th-order flux polynomial $f(x)$. The flux polynomial in each element is extrapolated to the interfaces, giving left and right flux states f_L and f_R on each side of the interface. A common numerical flux f^* is found at each interface using an approximate Riemann solver such as the Rusanov [40] or Roe method [30] for the inviscid flux and the local discontinuous Galerkin method [41] for the viscous flux. The next step is to construct a globally continuous flux polynomial. In the FR method, this is achieved by adding a flux correction polynomial Δf to the discontinuous flux $f(x)$. The correction satisfies 1) $f + \Delta f$ equals the common interface fluxes, and 2) the corrected flux optimally represents the discontinuous flux in the element interior. Δf is given by

$$\Delta f(x) = [f_L^* - f(-1)]g_L(x) + [f_R^* - f(1)]g_R(x) \quad (3)$$

where f_L^* , f_R^* are the common interface fluxes at left and right interfaces, and $g_L(x)$, $g_R(x)$ are order p polynomial correction functions satisfying $g_L(-1) = g_R(1) = 1$, $g_L(1) = g_R(-1) = 0$, $g_L(x) = g_R(-x)$. The corrected, globally C_0 -continuous flux f^C is given by $f^C = f + \Delta f$. To update the solution, the divergence of the continuous flux is calculated at the solution points (first, the flux is interpolated from the flux points to the solution points). An isoparametric mapping from the physical domain $x \in \Omega_j$ to the reference domain $\xi \in [-1, 1]$ is introduced:

$$\xi|_{\Omega_j}(x) = 2 \frac{x - x_j}{x_{j+1} - x_j} - 1 \quad (4)$$

where x_j, x_{j+1} are the endpoints of the element Ω_j . Now, denoting \mathbf{u}_j^δ as the discrete solution in element Ω_j and \mathbf{f}_j^δ as the discrete flux, the update step is written in semidiscrete form as

$$\begin{aligned} \frac{\partial \mathbf{u}_j^\delta}{\partial t} = & -J_j^{-1} [\mathbf{D}_j \mathbf{f}_j^\delta + (f^*(x_j) - f_j^\delta(x_j)) \mathbf{g}_{L,\xi} \\ & + (f^*(x_{j+1}) - f_j^\delta(x_{j+1})) \mathbf{g}_{R,\xi}] \end{aligned} \quad (5)$$

where J_j is the Jacobian in element Ω_j , $\mathbf{g}_{L,\xi}$ and $\mathbf{g}_{R,\xi}$ are the derivatives of the correction functions with respect to ξ at the solution points, and

$$\mathbf{D}_j = \frac{\partial l_j}{\partial \xi}$$

is the discrete derivative operator. The time derivative is discretized by an explicit fourth-order Runge–Kutta scheme, thus avoiding the need to construct and invert large matrices.

B. Energy-Stable Flux Reconstruction Schemes

We consider the 1-D conservation equation:

$$\frac{\partial u}{\partial t} + \frac{\partial}{\partial x} \left(f \left(u, \frac{\partial u}{\partial x} \right) \right) = 0 \quad (6)$$

where, in general, f is a nonlinear function. The second-order partial differential equation (PDE) is written as a system of first-order PDEs by introducing an auxiliary variable q :

$$\frac{\partial u}{\partial t} + \frac{\partial}{\partial x} (f(u, q)) = 0 \quad (7a)$$

$$q - \frac{\partial u}{\partial x} = 0 \quad (7b)$$

Now, the linear advection-diffusion equation is given by Eq. (7) with

$$f = au - b \frac{\partial u}{\partial x} \quad (8)$$

where a and b are constant scalars, and $b > 0$. It was proven by Castonguay et al. [15] that the FR schemes are energy stable for the linear advection-diffusion equation (Eq. 8) using an “energy method,” as was used to prove stability of the linear advection problem [14,42]. The schemes are energy stable if the following inequality is satisfied:

$$\frac{1}{2} \frac{d}{dt} \|U\|_{p,c}^2 + b \|Q\|_{p,\kappa}^2 \leq 0 \quad (9)$$

where $\|U\|_{p,c}$ and $\|Q\|_{p,\kappa}$ are broken Sobolev norms of the solution u and the auxiliary variable q , which are defined as follows:

$$\|U\|_{p,c} = \left\{ \sum_{n=1}^N \int_{x_n}^{x_{n+1}} \left[(u_n)^2 + \frac{c}{2} (J_n)^{2p} \left(\frac{du_n}{dx} \right)^2 \right] dx \right\}^{1/2} \quad (10a)$$

$$\|Q\|_{p,\kappa} = \left\{ \sum_{n=1}^N \int_{x_n}^{x_{n+1}} \left[(q_n)^2 + \frac{\kappa}{2} (J_n)^{2p} \left(\frac{dq_n}{dx} \right)^2 \right] dx \right\}^{1/2} \quad (10b)$$

Here, the constants c and κ parameterize the schemes. For $c \geq 0$ and $\kappa \geq 0$, $\|U\|_{p,c}$ and $\|UQ\|_{p,\kappa}$ are norms, and the schemes are guaranteed to be stable in accordance with Eq. (9). The proof of stability is quite general, as it ensures boundedness of the solution for all orders of accuracy, independent of the location of solution points within the 1-D element. It can then be shown that, to satisfy the stability condition, the correction functions g_L and g_R are given by

$$g_L = \frac{(-1)^p}{2} \left[L_p - \left(\frac{\eta_p(c) L_{p-1} + L_{p+1}}{1 + \eta_p(c)} \right) \right] \quad (11a)$$

$$g_R = \frac{1}{2} \left[L_p - \left(\frac{\eta_p(c) L_{p-1} + L_{p+1}}{1 + \eta_p(c)} \right) \right] \quad (11b)$$

where L_p is the degree p Legendre polynomial, $\eta_p(c) = (c(2p+1)(a_p p!))^2/2$, and $0 \leq c \leq \infty$ is the stability parameter in Eq. (10). If $c = c_{\text{NDG}} = 0$, then $\eta_p = 0$, implying

$$g_L = \frac{(-1)^p}{2}(L_p - L_{p+1}) \quad (12a)$$

$$g_R = \frac{1}{2}(L_p + L_{p+1}) \quad (12b)$$

which are the left and right Radau polynomials, respectively; hence, $c = 0$ recovers a particular FR-NDG scheme, as shown by Huynh [13]. The recovered scheme uses a collocation projection of the flux onto a polynomial space of degree p , which has significant implications for the nonlinear stability. The spectral difference (FR-SD) scheme can be recovered (for a linear flux) if the flux correction Δf is zero at a set of p points in the interior of the standard element [14]. The only way to satisfy this requirement is if $c = c_{SD}$, where c_{SD} is given by

$$c_{SD} = \frac{2p}{(2p + 1)(p + 1)(a_p p!)^2} \quad (13)$$

A third scheme, identified by Huynh as being particularly stable, is referred to as the G_2 scheme [13] and is recovered by choosing $c = c_{G2}$ given by

$$c_{G2} = \frac{2(p + 1)}{p(2p + 1)(a_p p!)^2} \quad (14)$$

In the general case of a nonlinear flux, it is well documented that high-order schemes suffer from aliasing-driven instabilities resulting from the projection of the flux onto a polynomial space of finite (p) dimensions [7]. It was shown by Allaneau and Jameson [32] that setting $c > 0$ in the ESRF schemes corresponds to damping of the highest-order polynomial mode by the application of a filter to the residual. In fact, filtering is a commonly used stabilization technique with NDG schemes [7,21,43]. Therefore, the FR formulation implicitly includes a stabilization mechanism. Furthermore, Jameson et al. [18] showed that the aliasing error associated with the ESRF schemes could be minimized in 1-D by choosing the solution points to be the Gaussian quadrature points. Williams and Jameson [19] devised new quadrature schemes in order to enhance nonlinear stability in simplex elements (triangles and tetrahedra).

C. Spectral Properties

Vincent et al. [33] performed a von Neumann analysis of the ESRF formulation, identifying dissipation and dispersion relations and calculating the order of accuracy as a function of c . Accuracy in this sense is correlated with the fraction of resolvable wave numbers for which waves are propagated with negligible dissipation and dispersion. Their analysis is summarized here. Consider the 1-D linear advection equation, Eq. (6) with $f = au$, where a is the advection speed, in coordinates x', t' . Let the grid be of uniform resolution h and nondimensionalize the equation with $x = x'/h$ and $t = t'/h$ so that we have

$$\frac{\partial u}{\partial t} + \frac{\partial u}{\partial x} = 0 \quad (15)$$

Since we know the direction of information propagation, we can fully upwind the flux, i.e., $f^*(x_j) = u^\delta(x_{j-1})$. Then, the update step [Eq. (5)] is rewritten as

$$\frac{\partial \mathbf{u}_j^\delta}{\partial t} = -J_j^{-1} [C_0 \mathbf{u}_j^\delta + C_{-1} \mathbf{u}_{j-1}^\delta] \quad (16a)$$

$$C_0 = D - \mathbf{g}_{L,\xi} \mathbf{l}_L^T \quad (16b)$$

$$C_{-1} = \mathbf{g}_{L,\xi} \mathbf{l}_R^T \quad (16c)$$

where $\mathbf{g}_{L,\xi}$ is the gradient of the left correction function, and \mathbf{l}_L and \mathbf{l}_R are vectors containing the values of the Lagrange polynomials on the left and right interfaces. An initial condition $u(x, 0) = e^{ikx}$ is specified that admits a solution of the form $u(x, t) = e^{ik(x-t)}$, where k is the wave number. The solution can be expressed in the parent domain using the mapping in Eq. (4):

$$u(x \in \Omega_j, t) = e^{ik(j-t)} e^{ik((\xi+1)/2)} \quad (17)$$

This infinite-dimensional exact solution must be projected to the finite-dimensional polynomial space to obtain the numerical solution

$$\mathbf{u}_j^\delta(t) = e^{ik(j-a^\delta(k)t)} \mathbf{v} \quad (18)$$

where $a^\delta(k)$ is the numerical wave speed as a function of wave number, and \mathbf{v} is the unknown vector associated with the projection. By introducing this numerical solution into the update step [Eq. (5)], we arrive at the semidiscrete dispersion relation

$$\mathbf{M} \mathbf{v} = a^\delta \mathbf{v} \quad (19a)$$

$$\mathbf{M} = \frac{-2i}{k} (C_0 + e^{-ik} C_{-1}) \quad (19b)$$

which is a $p + 1$ -dimensional eigenvalue problem for each wave number k . The solution of Eq. (19) provides $p + 1$ numerical modes for each k with the complex eigenvalues

$$a_p^\delta(k) = a_{p_r}^\delta(k) + ia_{p_i}^\delta(k), \quad p = 1, 2, \dots, p + 1 \quad (20)$$

where $a_{p_r}^\delta$ and $a_{p_i}^\delta$ are the real and imaginary numerical wave speeds, respectively. The analytical solution has the exact relation $a_r = 1$, $a_i = 0$; therefore, the errors associated with numerical dispersion and dissipation are $e^{ik(1-a_{p_r}^\delta, t)}$ and $e^{ika_{p_i}^\delta, t}$ respectively. The usual interpretation of the existence of multiple numerical modes for each wave number is that one mode is “physical,” in the sense that it most closely follows the analytical mode; whereas the remaining p of the $p + 1$ admissible modes are “spurious.” These spurious modes are often neglected by assuming that they contain only a small fraction of the energy and are fairly dissipative [33]. The reader is referred to Asthana and Jameson [34] for a comprehensive discussion of the spurious modes.

Figure 2 plots the real and imaginary components of the physical mode against the normalized wave number $k/(p + 1)$ for the FR-NDG scheme for polynomial orders from one to five (p_1 to p_5). The real part is plotted as the effective wave number $k_{\text{eff}} = a_r^\delta k/(p + 1)$, and the imaginary part $a_{p_i}^\delta$ is plotted directly. The components of exact wave speed, a_r and a_i , are plotted for reference. As p is increased, the exact solution is approximately followed over a larger proportion of the range of resolvable wave numbers. However, the overshoot in the dispersion relation becomes more pronounced, implying a lower CFL limit. Dissipation is reduced at higher p , which translates as better resolving efficiency. Figure 3 plots the real and imaginary components of the physical mode for FR-NDG, FR-SD, and Huynh’s G_2 scheme [13] at order p_3 . The effect of changing c from $c = c_{NDG} = 0$ to $c = c_{SD}$ is that the numerical wave speed remains closer to the exact wave speed for longer, but the dissipation starts increasing (i.e., $a_{p_i}^\delta < 0$) at a lower normalized wave number, suggesting that an optimal scheme might exist in between FR-NDG and FR-SD. The G_2 scheme is inferior to FR-SD in terms of both errors.

D. Optimized FR Schemes

Recently, Asthana and Jameson [34] carried out an optimization of the ESRF schemes in spectral space using c as the free parameter.

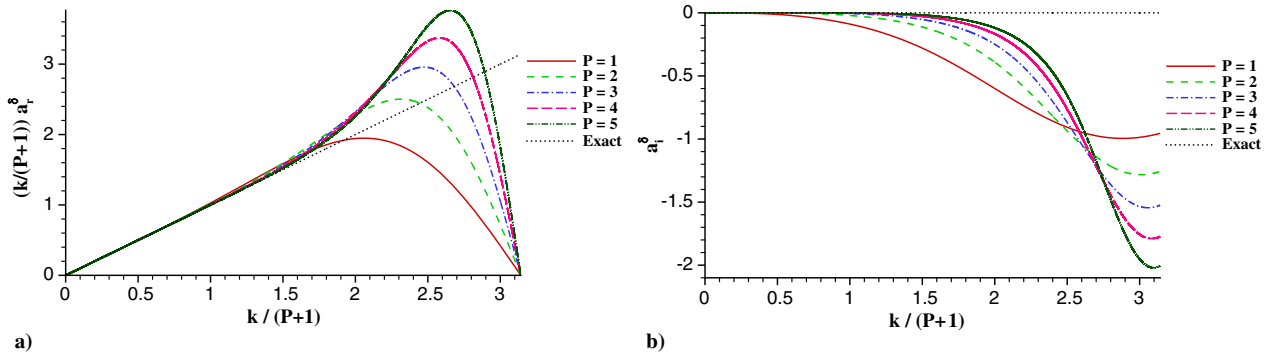


Fig. 2 Effect of p on a) k_{eff} and b) a_i^δ for FR-NDG scheme (from Asthana and Jameson).

They identified an optimal value of c at each order p for which the dissipation and dispersion errors were minimized over the range of resolvable wave numbers, denoting the scheme as the OESFR scheme. Optimizing with respect to both errors balanced the competing effects described previously, finding a minimum close to $c = c_{\text{NDG}} = 0$. They then tackled the more complex multidimensional optimization problem of finding the zeros of the correction functions, which minimized the dissipation and dispersion errors. A general form of the left correction function was considered:

$$g_L(\xi) = \prod_{n=1}^p \frac{\xi - \xi_n}{1 + \xi_n} \frac{\xi - 1}{2} \quad (21)$$

which ensured a unity value on the left interface; the right correction function g_R is simply a mirror of g_L . The p -dimensional solution space of free zeros $\{\xi_1, \xi_2, \dots, \xi_{p+1}\}$ contains the family of ESFR schemes as a subspace. The so-called optimal FR schemes could then be identified subject to the constraint that they are linearly stable. For

$p = 1$, the OESFR scheme was recovered owing to the single degree of freedom but, for $p > 1$, the schemes were outside the ESFR family. Figure 4 plots the dispersion and dissipation relations for FR-NDG, OESFR, and OFR for p_4 . The OESFR scheme has a slightly lower dispersion error than FR-NDG and an almost identical dissipation error, whereas for the OFR scheme, both errors are significantly lower than FR-NDG.

E. FR Schemes for Turbulent Flow Simulations

The ESFR schemes have been used successfully for implicit large-eddy simulation of a number of challenging turbulent flows, including transitional flow over an SD7003 airfoil at $Re_C = 60,000$ [44], transitional flow over a pitching and plunging NACA 0012 wing section [45], and unsteady flow over a flapping wing–fuselage configuration [46]. Closure of the underresolved Navier–Stokes equations was handled in these cases by numerical dissipation emanating from the upwinded interface fluxes. Equipped with an LES model, they have also been used to accurately simulate the

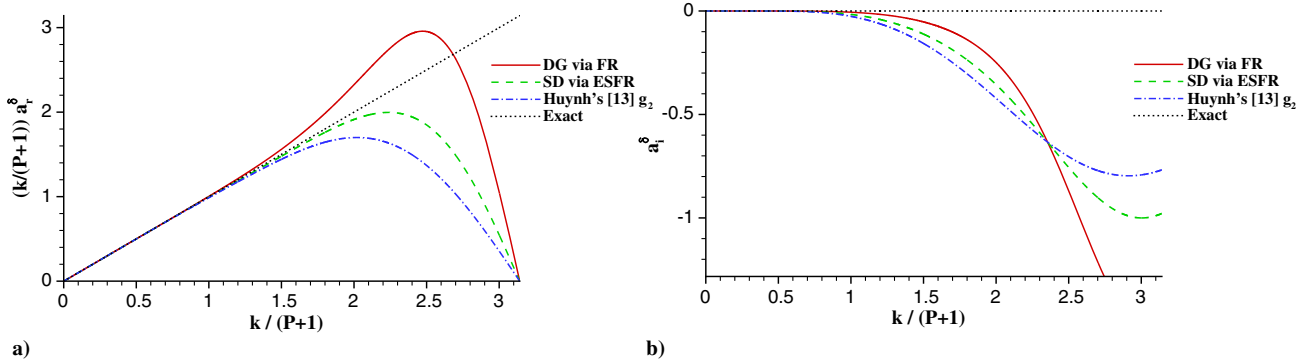


Fig. 3 Representations of a) k_{eff} and b) a_i^δ for p_3 FR-NDG, FR-SD, and G_2 schemes (from Asthana and Jameson).

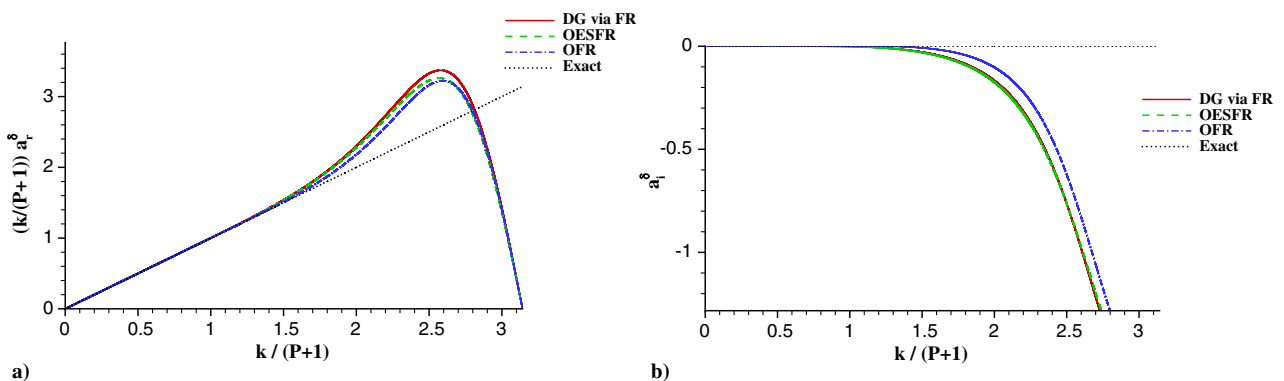
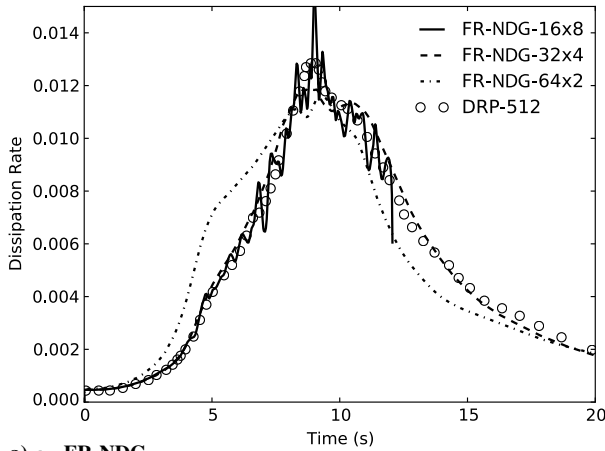


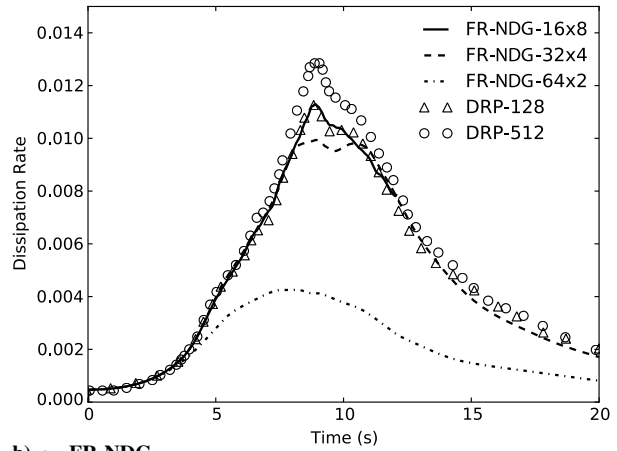
Fig. 4 Representations of a) k_{eff} and b) a_i for p_4 FR-NDG, OESFR, and OFR schemes (from Asthana and Jameson).

turbulent flow over a square cylinder at $Re = 21,400$ on relatively coarse hexahedral [47] and tetrahedral [38] meshes. Nevertheless, there remain open questions about the schemes' behaviors in underresolved turbulent flows. It is not known which are the most accurate schemes in terms of faithfully capturing as much of the turbulent spectrum as possible when the grid resolution is larger than the Kolmogorov length scale. Unfortunately, it is likely that the most accurate scheme will not be the most stable, and so the question needs to be rephrased as follows: "Which scheme has the best balance of accuracy and stability?" The results presented in the previous section encourage the use of the newly developed OFR scheme for turbulent flow simulations, where the improvements in spectral accuracy over

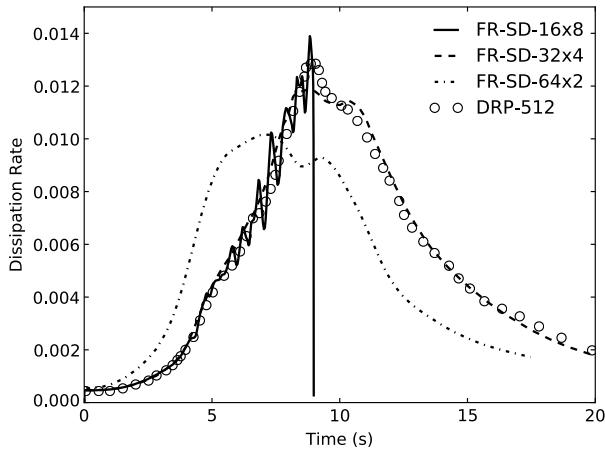
FR-NDG and FR-SD should be visible, particularly on coarse meshes where the full spectrum cannot be fully resolved. It is also important to examine the role of polynomial order in simulations of turbulent flows. To take full advantage of high-order schemes over second-order schemes including computational efficiency, we wish to use a high polynomial order. The aforementioned spectral results imply that higher orders provide better spectral resolution and lower numerical dissipation. Yet, as the order is increased, it was found that aliasing instabilities grew large in simulations of the Taylor–Green vortex [38]. Furthermore, the reduced CFL limits at higher orders might reduce the computational efficiency due to the resulting longer simulation times.



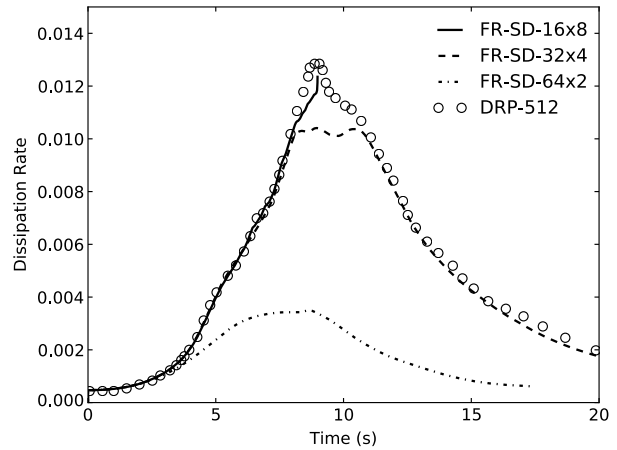
a) ϵ_1 , FR-NDG



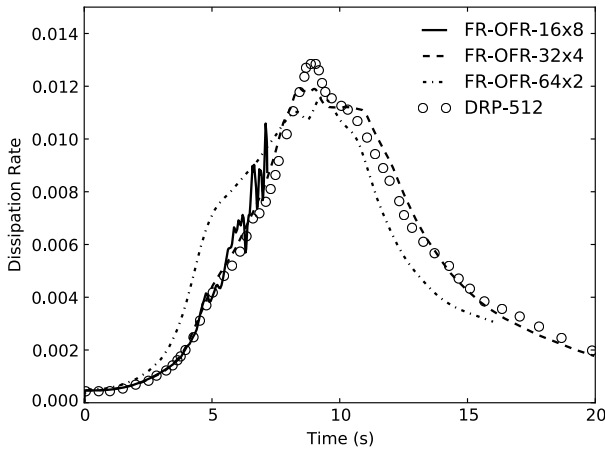
b) ϵ_2 , FR-NDG



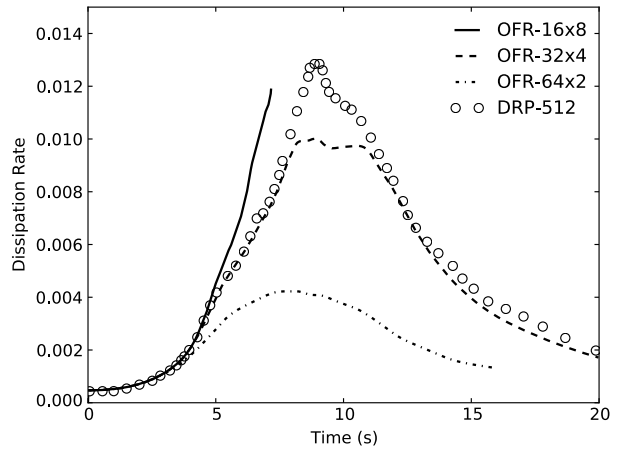
c) ϵ_1 , FR-SD



d) ϵ_2 , FR-SD



e) ϵ_1 , OFR



f) ϵ_2 , OFR

Fig. 5 Representations of a, c, e) ϵ_1 and b, d, f) ϵ_2 using FR-NDG, FR-SD, and OFR schemes with 128^3 DOFs. DRP-128, DRP-512 denote DRP scheme on 128^3 - and 512^3 -DOF meshes, respectively.

III. Taylor–Green Vortex

The Taylor–Green vortex problem is a canonical flow that provides a convenient stepping stone toward simulating real flows, requiring the solution of the Navier–Stokes equations in 3-D at moderate Reynolds numbers. From a simple initial datum, vortex stretching mechanisms cause the flow to decay along a well-defined trajectory, generating a detailed turbulent spectrum over a period of 20 s. The TGV was one of the problems in the first, second, and third international workshops on high-order CFD methods and is considered to be a challenging test for high-order methods. Various authors have used high-order discontinuous methods on the TGV test case with excellent results, including classical DG [5,36,37], DGSEM, [9,29] and a preliminary study by Bull and Jameson using the FR-SD scheme [38]. Wang et al. gave a review of the current status of high-order methods for several problems including the TGV [1]. In this paper, we use the TGV case to test the ability of various FR schemes to accurately represent the turbulent spectrum and examine the nonlinear stability of these schemes at varying orders of approximation.

A. Problem Setup

The geometry is a triply periodic box of dimension $0 \leq (x, y, z) \leq 2\pi$, and the initial condition is given by the following:

$$u(t_0) = u_0 \sin(x/L) \cos(y/L) \cos(z/L) \quad (22)$$

$$v(t_0) = -u_0 \cos(x/L) \sin(y/L) \cos(z/L) \quad (23)$$

$$w(t_0) = 0 \quad (24)$$

$$p(t_0) = p_0 + \frac{\rho_0}{16} \left[\cos\left(\frac{2x}{L}\right) + \cos\left(\frac{2y}{L}\right) \right] \left[\cos\left(\frac{2z}{L}\right) + 2 \right] \quad (25)$$

where $L = 1$, $u_0 = 1$, $\rho_0 = 1$, and $p_0 = 100$. The Mach number is set to 0.08 (consistent with the initial pressure p_0), and the initial temperature is 300 K. A Reynolds number of 1600 is prescribed by adjusting the viscosity. Three meshes are used: a coarse mesh of 16^3 hexahedral elements, a medium mesh (32^3 elements), and a fine mesh (64^3 elements). We compare our results to several others submitted to the First High-Order Workshop. A high-resolution reference solution was computed by Debonis [48] using Bogey and Bailey’s 13-point dispersion-relation-preserving (DRP) scheme [49] on a mesh of 512^3 elements. Debonis used the same scheme on meshes of 64^3 , 128^3 , and 256^3 elements [48]; and we also compare our results to these. The closest published results in terms of using a similar method are those of Beck and Gassner, who used a filtered fourth-order-accurate DGSEM on a 64^3 element mesh [9]. These are also plotted in some figures for comparison. Energy spectra are compared to a pseudospectral computation on a 512^3 element mesh computed by Carton de Wiart et al. [37].

B. Diagnostics

Several diagnostic quantities can be computed from the flow as it evolves in time, allowing the characteristics of the numerical scheme to be observed. First, the volume-averaged kinetic energy is given by

$$E_k = \frac{1}{\rho_0 V} \int_V \frac{1}{2} \rho \mathbf{u} \cdot \mathbf{u} \, dV \quad (26)$$

where V is the volume. Now, we can compute the rate of dissipation from the kinetic energy:

$$\epsilon_1 = \epsilon(E_k) = -\frac{dE_k}{dt} \quad (27)$$

This quantity ϵ_1 is referred to as the energy-based dissipation rate. In incompressible flow, it can be shown that the dissipation rate is related to the integrated enstrophy ζ by a constant [35]:

$$\epsilon_2 = \epsilon(\zeta) = \frac{2\mu}{\rho_0} \zeta \quad (28)$$

$$\zeta = \frac{1}{\rho_0 V} \int_V \frac{1}{2} \rho \boldsymbol{\omega} \cdot \boldsymbol{\omega} \, dV \quad (29)$$

where $\boldsymbol{\omega}$ is the vorticity, and μ is the dynamic viscosity. Since the Mach number of the TGV case is low, Eq. (28) can be assumed to hold true. We refer to ϵ_2 as the vorticity-based dissipation. In compressible flow, the dissipation rate is given by the sum of three components ϵ_3 , ϵ_4 , and ϵ_5 given by

$$\epsilon_3 = \epsilon(\mathbf{S}) = 2 \frac{\mu}{\rho_0 V} \int_V \mathbf{S} : \mathbf{S} \, dV \quad (30)$$

$$\epsilon_4 = \epsilon(\mu_v) = \frac{\mu_v}{\rho_0 V} \int_V (\nabla \cdot \mathbf{u})^2 \, dV \quad (31)$$

$$\epsilon_5 = \epsilon(p) = -\frac{1}{\rho_0 V} \int_V p \nabla \cdot \mathbf{u} \, dV \quad (32)$$

where $\mu_v = 0$ is the bulk viscosity (thus ϵ_4 is neglected), and \mathbf{S} is the rate-of-strain tensor [35]. The pressure dilatation-based dissipation rate ϵ_5 drops out in the incompressible limit and is expected to be small at Mach 0.08. Therefore, the strain-based dissipation rate ϵ_3 is expected to be almost identical to ϵ_2 .

The vorticity-based dissipation rate is a measure of how well the vorticity-carrying small scales (i.e., the inertial range of turbulence) are resolved, and it is considered to be a sensitive measure of how accurately turbulence is resolved by a numerical method. Numerical dissipation reduces the sharpness with which velocity gradients are approximated [35]. It can be estimated by the difference between ϵ_1 and ϵ_2 and will be nonzero for any method that is not kinetic-energy preserving [1,37]. This is a useful error measure, in that it is

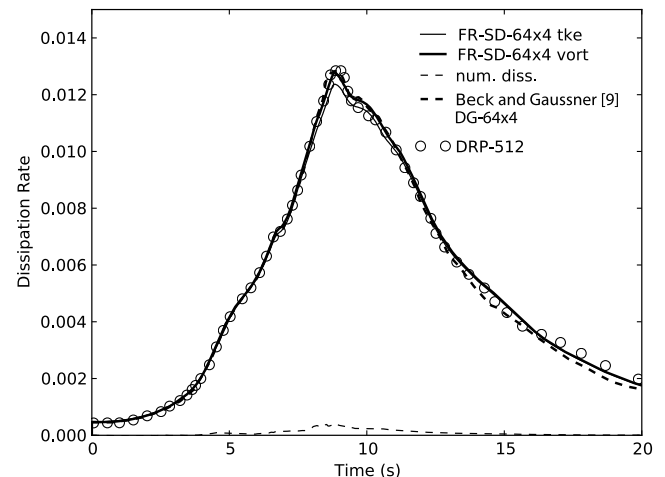


Fig. 6 ϵ_1 , ϵ_2 , and $\epsilon_1 - \epsilon_2$ using FR-SD at p_3 on fine mesh.

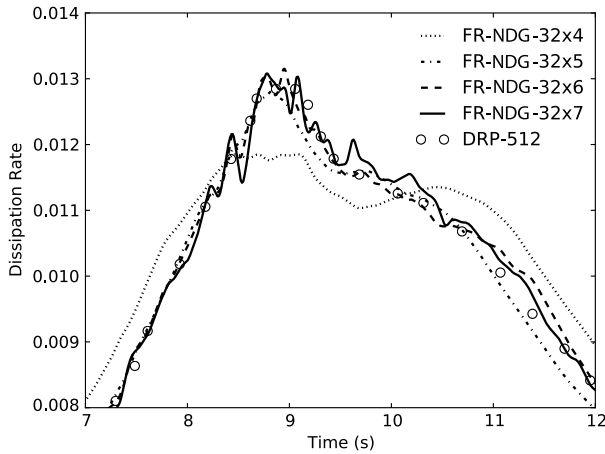
independent of the reference solution and could be used in more complex flows [1].

C. Results

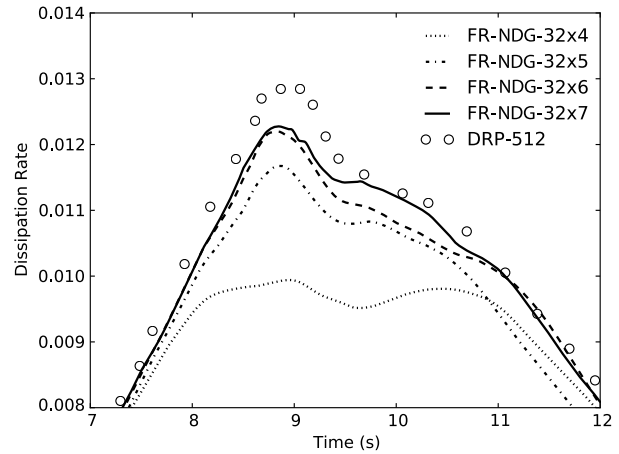
1. Effect of Polynomial Order

To illustrate the effect of polynomial order on the accuracy and stability of the solution, Fig. 5 shows energy-based dissipation rate ϵ_1 and vorticity-based dissipation rate ϵ_2 using FR-NDG (Figs. 5a and 5b), FR-SD (Figs. 5c and 5d), and OFR (Figs. 5e and 5f) at a constant 128 degrees of freedom (DOFs) per direction given by p_7 on the coarse, p_3 on the medium, and p_1 on the fine meshes (denoted 16×8 ,

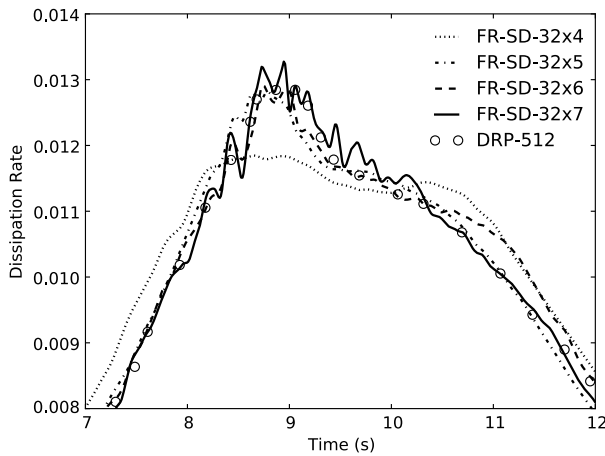
32×4 , and 64×2 DOFs in the figure). The OESFR scheme obtained identical results to FR-NDG because c_{OESFR} is very close to $c_{\text{NDG}} = 0$; therefore, the OESFR results are not shown here. A reference ϵ_2 solution from the high-order workshop computed by Debonis [48] using the DRP scheme on a 512^3 element mesh is also plotted, denoted by “DRP-512” (note that, at this high level of resolution, ϵ_1 and ϵ_2 are equal, so it is not necessary to plot the reference ϵ_1 solution as well). Also included in Fig. 5b is a reference ϵ_2 solution with an equivalent number of DOFs to the current results, namely, the DRP scheme on a 128^3 mesh computed by Debonis [48], denoted by “DRP-128.”



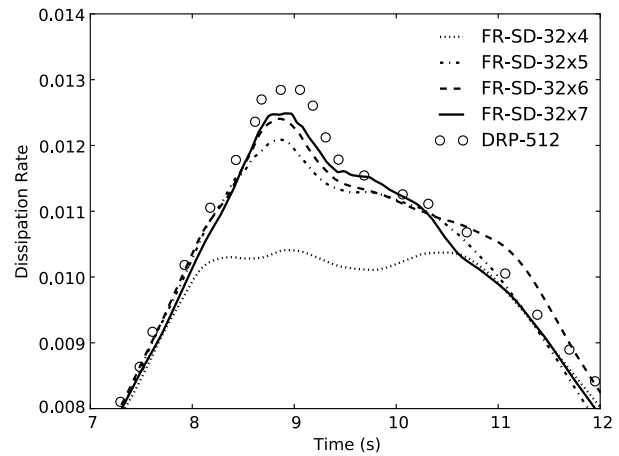
a) ϵ_1 , FR-NDG



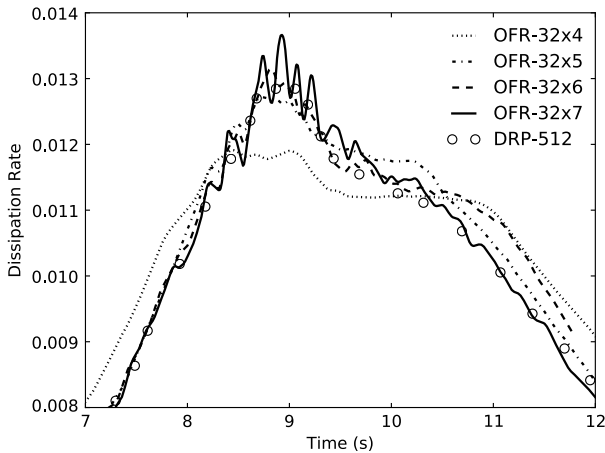
b) ϵ_2 , FR-NDG



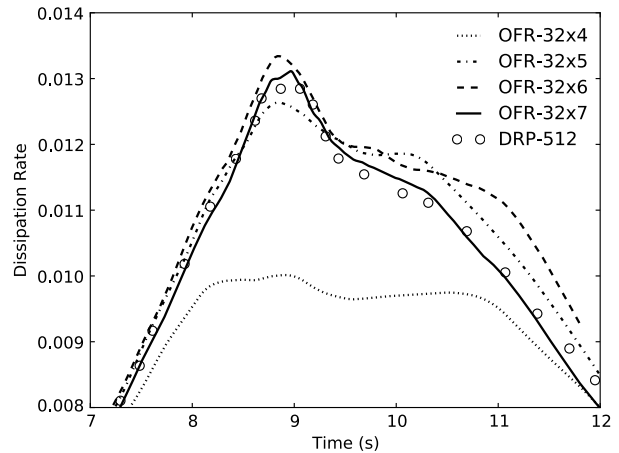
c) ϵ_1 , FR-SD



d) ϵ_2 , FR-SD



e) ϵ_1 , OFR



f) ϵ_2 , OFR

Fig. 7 Representations of a, c, e) ϵ_1 and b, d, f) ϵ_2 using FR-NDG, FR-SD, and OFR at p_3, p_4, p_5 , and p_6 on medium mesh.

We can observe the competing effects of stability and accuracy: the low-order p_1 solutions on the fine mesh are inaccurate due to excessive dissipation, whereas the high-order p_7 solutions on the coarse mesh oscillate before diverging (FR-NDG at $t \approx 12$, FR-SD at $t \approx 9$, and OFR at $t \approx 7.5$). It is apparent that, at p_7 , the OFR scheme is the least stable because it diverged the earliest. The overprediction of ϵ_2 by this scheme is indicative of too little dissipation in the smallest resolved scales. The ‘‘Goldilocks’’ solutions [p_3 on the medium mesh (32×4)] have a good balance of accuracy and stability. The oscillations in the p_7 solutions are thought to be caused by representing the flow structures with high-order polynomials, which naturally contain large variations. In a real turbulent flow, one expects these variations to disappear when considering average quantities over a sufficiently large volume. However, the TGV flow has several symmetries so that variations occurring simultaneously in different parts of the flow may add up. These results confirm that some means of dealiasing are essential for very high-order FR schemes (in particular, the low-dissipation OFR scheme) when the flow is underresolved. However, in order to preserve the accuracy of the schemes, stabilization should only be added when and where necessary to control the growth of oscillations. For example, filtering could be applied to individual elements or even solution points according to a shock sensor [50]. This approach is being developed for the FR schemes by Sheshadri and Jameson [51]. The results also show that ϵ_2 is a more sensitive measure of accuracy, but ϵ_1 is a more sensitive measure of stability.

Figure 6 plots ϵ_1 and ϵ_2 from the p_3 FR-SD solution on the fine mesh (denoted ‘‘tke’’ and ‘‘vort.’’ respectively) versus the DRP-512 solution and a solution with an equivalent number of DOFs, namely, filtered fourth-order DGSEM on a 64^3 mesh computed by Beck and Gassner [9]. The numerical dissipation of the FR scheme (denoted as ‘‘num. diss.’’), given by $\epsilon_1 - \epsilon_2$, is also plotted. The variable ϵ_1 given by FR-SD almost exactly matches the reference solutions with no oscillations, providing further evidence that fourth-order FR schemes strike the right balance between accuracy and stability. The numerical dissipation is small, indicating that the majority of the kinetic energy loss is via molecular dissipation, as observed by Beck and Gassner [9].

2. Effect of FR Scheme

Figures 7a, 7c, and 7e show close-ups of the peak of ϵ_1 computed using the FR-NDG, FR-SD, and OFR schemes at orders p_3 to p_6 on the medium mesh versus the DRP-128 and DRP-512 solutions. At p_3 , all the schemes behave in a similar manner, underpredicting the peak. At p_4 and p_5 , all the schemes capture the peak fairly well, but small oscillations appear in the p_5 solutions. The p_6 solutions all display significant oscillations close to $t = 9$. When the three schemes at orders p_3 to p_6 were used on the coarse mesh (results not shown), only the FR-NDG scheme did not diverge at orders p_5 and p_6 , suggesting that FR-NDG is the most stable scheme (of those tested) at low resolution.

Figures 7b, 7d, and 7f show close-ups of the peak of the vorticity-based dissipation rate ϵ_2 computed using the same schemes and orders as Figs. 7a, 7c, and 7e. As in Fig. 5, differences in accuracy between the schemes are much more visible than in the ϵ_1 plots. FR-NDG underpredicts the peak at all orders, FR-SD underpredicts the peak slightly less, and OFR predicts the peak fairly accurately at orders greater than p_3 . The p_6 OFR solution matches the reference data very well. The slight overprediction of ϵ_2 (i.e., vorticity strength) by the p_5 OFR scheme is suggestive of excess energy in the small resolved scales. This is observed to a greater degree in the seventh-order OFR solution in Fig. 5f. In the case of a nonlinear flux, it is known that the aliasing error causes energy to pile up in the scales near the grid scale due to inadequate draining by the numerical scheme or by molecular viscosity when the grid is coarse [52]. In Sec. II.C, the OFR scheme was shown to have reduced numerical dissipation compared to FR-NDG or FR-SD at high wave numbers, implying a smaller drain of the energy and an over-prediction of vorticity. Nevertheless, these results using the new OFR scheme confirm that the theoretically superior greater accuracy is indeed borne out in practice.

3. Compressibility Effects

The dissipation rate due to pressure dilatation ϵ_5 measures the effect of compressibility on the dissipation of turbulent energy. Figure 8 plots ϵ_5 for the FR-NDG, FR-SD, and OFR schemes at p_4 on the medium mesh versus the DRP scheme on the 64^3 and 512^3 meshes. As the Mach number is so low, the effects of compressibility should not be very strong and ϵ_5 is expected to be close to zero (as is the case with the DRP scheme). Note that the y-axis scale is stretched by a factor of 100 compared to the previous plots. Despite having 2.5 times the number of DOFs per direction, the magnitude of the variations in ϵ_5 using FR-NDG, FR-SD, and OFR are larger than those in the DRP solutions. The OFR results display the largest variations, possibly due to the lower numerical dissipation. At higher orders (not shown), it was found that all the FR schemes greatly overpredicted the magnitude of ϵ_5 and that the sign of ϵ_5 depended on the parity of the polynomial order. The root cause of these issues is thought to be related to the representation of the divergence term in Eq. (32) and is the subject of ongoing investigation. Nevertheless, ϵ_5 predicted by the FR schemes was found to converge to the correct solution with grid refinement, as was also observed by Chapelier et al. [5].

4. Energy Spectra

Figures 9a–9f displays energy spectra of the p_3 (Figs. 9a and 9b), p_4 (Figs. 9c and 9d), and p_5 (Figs. 9e and 9f) FR-NDG, FR-SD, and OFR solutions on the coarse and medium meshes at time $t = 9$ s compared to the reference solution computed using a pseudospectral method on a 512^3 mesh by Carton de Wiart et al. [37]. Note that the p_5 FR-SD scheme on the coarse mesh is not displayed because it diverged before $t = 9$ seconds. The maximum resolvable wave number on each mesh/order pairing, given by $k_{\max} = \text{DOF}/2$, is marked by a vertical dashed line. Significant discrepancies are observed at low wave numbers between the coarse-mesh results and the reference solution, caused by poor representation of the flow dynamics at such low resolution. Similar effects were also observed by Beck and Gassner at low resolution [9]. The energy in the highest resolvable wave numbers falls off short of k_{\max} in the p_3 and p_4 spectra with all schemes, whereas at p_5 , the spectra are much closer to the reference solution. This suggests that higher polynomial orders are better at maintaining the energy content of the smaller scales on low-resolution meshes. Looking only at the medium-mesh results, at p_3 , all the schemes produce similar spectra. As the order is increased, the differences between each scheme becomes more pronounced. The p_5 OFR spectra are much closer to the reference solution than the FR-NDG and FR-SD spectra; indeed, the p_5 OFR spectrum on the medium mesh overlies the reference spectrum for most of the resolvable range of wave numbers. It can be concluded that, as predicted by theory, the OFR scheme offers superior spectral resolution versus the FR-NDG and FR-SD schemes in practice, although the validity of this claim must also be verified in more complex test cases.

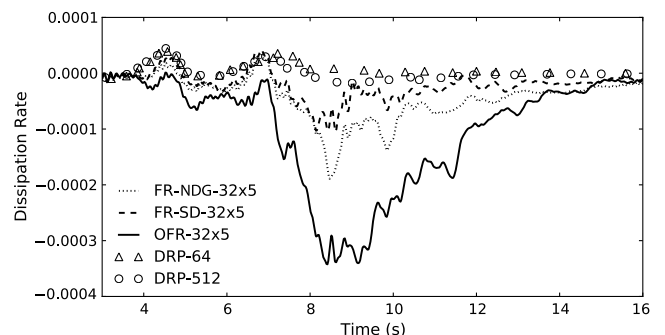


Fig. 8 Pressure dilatation-based dissipation rate ϵ_5 using FR-NDG, FR-SD, and OFR at p_4 on medium mesh.

5. Flow Visualization

Figure 10 shows contours of instantaneous vorticity magnitude $|\omega|$ on a small section of the plane defined by $x = 0$ at time $t = 8$, when the most complex vortical flow structures are generated. The reference data (solid black contours) were computed using a spectral element method with 512^3 DOFs by Carton de Wiart et al. [37] and are available from the 3rd High-order Workshop. The

solution obtained with the p_3 FR-NDG scheme on the fine mesh (filled contours with dashed divisions) is superimposed on the reference solution. Both sets of contours are defined by $|\omega| = \{1, 5, 10, 20, 30\}$. The FR-NDG solution approximately overlies the reference solution, but there are some discrepancies and noisy regions, possibly caused by the discontinuous nature of the solution and the relatively coarse mesh.

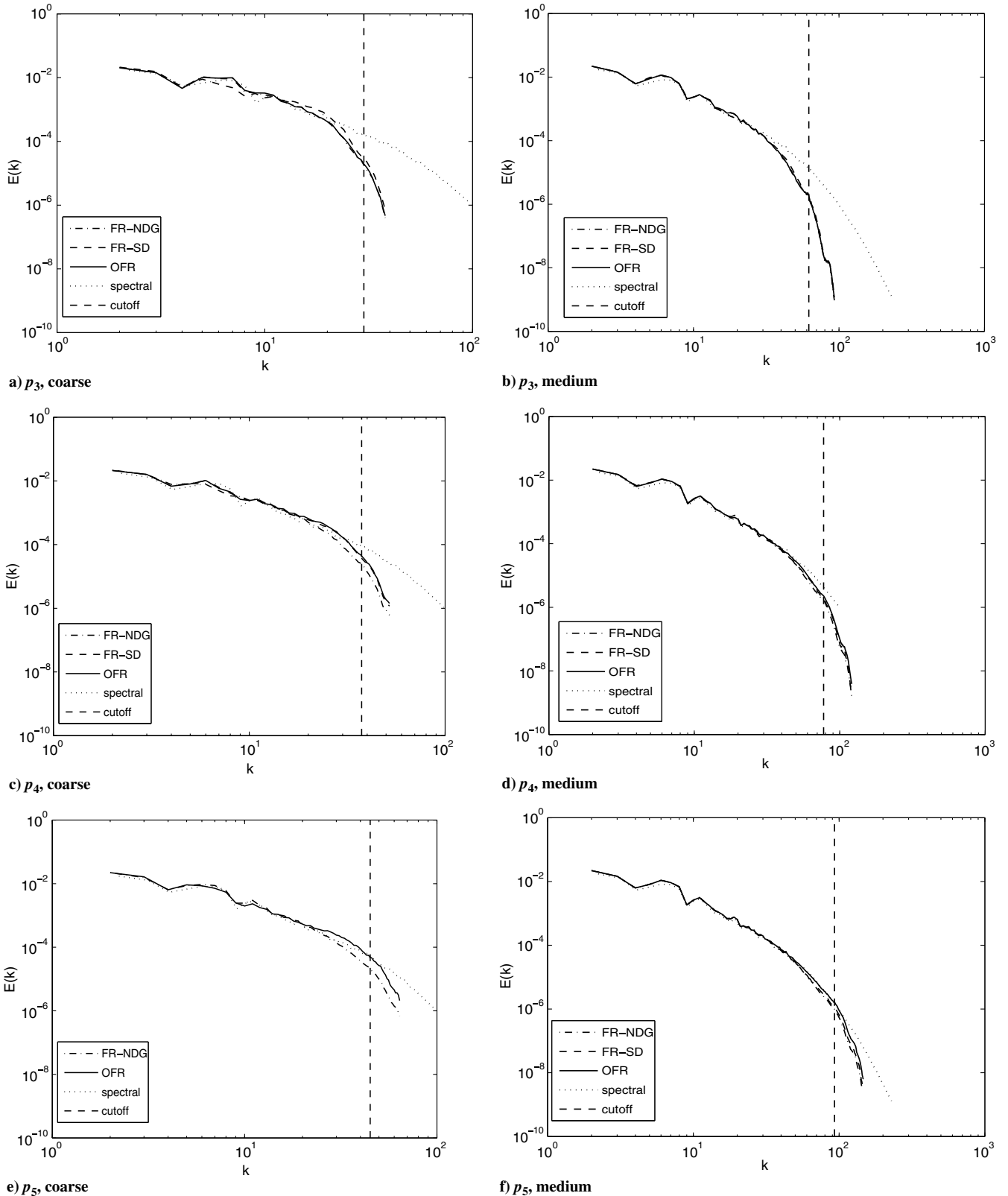


Fig. 9 Energy spectra of FR-NDG, FR-SD and OFR schemes at $t = 9$ at a, b) p_3 , c, d) p_4 , e, f) p_5 vs reference solution [37].

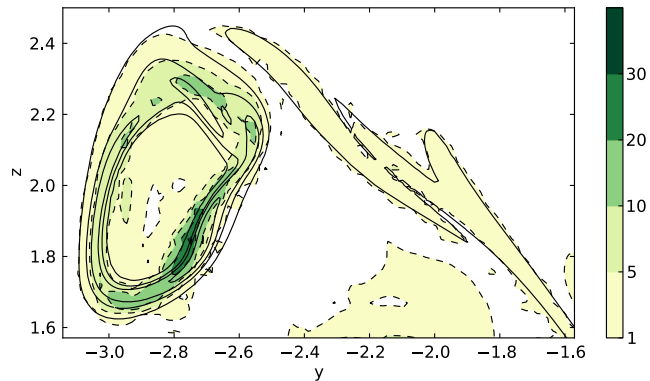


Fig. 10 Contours of vorticity on the plane $x = 0$ for p_3 FR-NDG on fine mesh (- -) and reference solution (—) [37].

IV. Conclusions

In this paper, the performance of the energy-stable flux reconstruction schemes and the optimized OESFR/OFR schemes in simulations of underresolved turbulent flow was investigated. The Taylor–Green vortex problem at $Re = 1600$ was simulated on a range of coarse meshes and polynomial orders using energy-stable flux reconstruction schemes encompassing the FR-NDG, FR-SD, optimized ESFR, and optimized FR schemes. Predictions of the energy-based dissipation rate ϵ_1 and vorticity-based dissipation rate ϵ_2 showed that a balance must be struck between accuracy and stability. Holding the number of DOFs constant, low-order p_1 schemes on a fine mesh were inaccurate but stable due to high numerical dissipation, whereas high-order p_7 schemes on a coarse mesh were more accurate but unstable. Fourth-order-accurate p_3 schemes offered a good balance of accuracy and stability; the p_3 FR-SD scheme on a mesh of 64^3 elements (i.e., 256 DOFs per direction) matched the reference solution. Instabilities in the solution at high orders are thought to originate from large variations in the high-order polynomials within each element coupled with aliasing errors and accumulation of energy in the small scales. Further work is needed to develop effective nonlinear stabilization techniques such as filtering; current research in the Aerospace Computing Laboratory is directed at this purpose.

All the FR schemes tested were able to fairly accurately predict ϵ_2 at orders of p_4 and above on a relatively coarse mesh, which is encouraging for their use in underresolved simulations of high-Reynolds-number turbulent flows. The DG and OESFR schemes, which behaved in an identical manner in all tests, were the least accurate. The FR-SD scheme was slightly more accurate and the OFR scheme was the most accurate, achieving excellent agreement with the reference solution at p_6 . The dissipation due to compressibility effects ϵ_5 was overpredicted by all the FR schemes at low resolution. It appears likely that instabilities associated with high-order polynomials are at the root of the problem, which will be the subject of future research. The energy spectra computed from the OFR results were in good agreement with the reference spectral solution of Carton de Wiart et al. [37] and were superior at high wave numbers to the spectra of FR-NDG and FR-SD results. This demonstrates that the optimization of the FR correction functions for wave propagation by Asthana and Jameson [34] is effective when applied to the unsteady Navier–Stokes equations in three dimensions and motivates the future use of the OFR scheme for more complex turbulent flows. These results show that flux reconstruction is a very promising method for simulating turbulent flows on coarse meshes. More research is needed to increase stability at high orders by draining energy from the highest resolved wave numbers. Future work will employ the FR schemes for LES of complex high-Reynolds-number flows.

Acknowledgments

This research was made possible by the support of the National Science Foundation under grant number 1114816, monitored by

Leland Jameson; and the U.S. Air Force Office of Scientific Research under grant number FA9550-10-1-0418, monitored by Fariba Fahroo.

References

- [1] Wang, Z., Fidkowski, K., Abgrall, R., Bassi, F., Caraeni, D., Cary, A., Deconinck, H., Hartmann, R., Hillewaert, K., Huynh, H., Kroll, N., May, G., Persson, P.-O., van Leer, B., and Visbal, M., “High-Order CFD Methods: Current Status and Perspective,” *International Journal for Numerical Methods in Fluids*, Vol. 72, No. 8, 2013, pp. 811–845. doi:10.1002/ld.3767
- [2] Lele, S., “Compact Finite Difference Schemes with Spectral-Like Resolution,” *Journal of Computational Physics*, Vol. 103, No. 1, 1992, pp. 16–42. doi:10.1016/0021-9991(92)90324-R
- [3] Bassi, F., and Rebay, S., “A High-Order Accurate Discontinuous Finite Element Method for the Numerical Solution of the Compressible Navier–Stokes Equations,” *Journal of Computational Physics*, Vol. 131, No. 2, 1997, pp. 267–279. doi:10.1006/jcph.1996.5572
- [4] Cockburn, B., Karniadakis, G., and Shu, C., *Discontinuous Galerkin Methods: Theory, Computation and Applications*, Springer, New York, 2000.
- [5] Chapelier, J.-B., Plata, M., and Renac, F., “Inviscid and Viscous Simulations of the Taylor–Green Vortex Flow Using a Modal Discontinuous Galerkin Approach,” *42nd AIAA Fluid Dynamics Conference and Exhibit*, AIAA Paper 2012-3073, June 2012.
- [6] Birken, P., Gassner, G., Haas, M., and Munz, C., “Efficient Time Integration for Discontinuous Galerkin Method for the Unsteady 3-D Navier–Stokes Equations,” *European Congress on Computational Methods and Applied Sciences and Engineering (ECCOMAS 2012)*, edited by Eberhardsteiner, J., et al., Vienna, Austria, 2012, <http://www.mathematik.uni-kassel.de/~birken/BirkenGassnerHaasMunzECCOMAS12.pdf>.
- [7] Hesthaven, J., and Warburton, T., *Nodal Discontinuous Galerkin Methods: Algorithms, Analysis, and Applications*, Vol. 54, Springer, New York, 2007.
- [8] Kopriva, D., *Implementing Spectral Methods for Partial Differential Equations: Algorithms for Scientists and Engineers*, 1st ed., Springer, New York, 2009.
- [9] Beck, A., and Gassner, G., “On the Accuracy of High-Order Discretizations for Underresolved Turbulence Simulations,” *Theoretical and Computational Fluid Dynamics*, Vol. 27, Nos. 3–4, 2012, pp. 221–237. doi:10.1007/s00162-011-0253-7
- [10] Gassner, G., Lorcher, F., Munz, C., and Hesthaven, J., “Polymorphic Nodal Elements and Their Application in Discontinuous Galerkin Methods,” *Journal of Computational Physics*, Vol. 228, No. 5, 2009, pp. 1573–1590. doi:10.1016/j.jcp.2008.11.012
- [11] Kopriva, D. A., and Koliass, J. H., “A Conservative Staggered-Grid Chebyshev Multidomain Method for Compressible Flows,” *Journal of Computational Physics*, Vol. 125, No. 1, 1996, pp. 244–261. doi:10.1006/jcph.1996.0091
- [12] Liu, Y., Vinokur, M., and Wang, Z. J., “Spectral Difference Method for Unstructured Grids I: Basic Formulation,” *Journal of Computational Physics*, Vol. 216, No. 2, 2006, pp. 780–801. doi:10.1016/j.jcp.2006.01.024
- [13] Huynh, H., “A Flux Reconstruction Approach to High-Order Schemes Including Discontinuous Galerkin Methods,” *18th AIAA Computational Fluid Dynamics Conference*, AIAA Paper 2007-4079, 2007.
- [14] Vincent, P. E., Castonguay, P., and Jameson, A., “A New Class of High-Order Energy Stable Flux Reconstruction Schemes,” *Journal of Scientific Computing*, Vol. 47, No. 1, 2011, pp. 50–72. doi:10.1007/s10915-010-9420-z
- [15] Castonguay, P., Williams, D., Vincent, P. E., and Jameson, A., “Energy Stable Flux Reconstruction Schemes for Advection–Diffusion Problems,” *Computer Methods in Applied Mechanics and Engineering*, Vol. 267, Dec. 2013, pp. 400–417. doi:10.1016/j.cma.2013.08.012
- [16] Williams, D. M., Castonguay, P., Vincent, P. E., and Jameson, A., “Energy Stable Flux Reconstruction for Advection–Diffusion Problems on Rtriangles,” *Journal of Computational Physics*, Vol. 250, Oct. 2012, pp. 53–76. doi:10.1016/j.jcp.2013.05.007
- [17] Williams, D. M., and Jameson, A., “Energy Stable Flux Reconstruction for Advection–Diffusion Problems on Tetrahedra,” *Journal of Scientific Computing*, Vol. 59, No. 3, 2013, pp. 721–759. doi:10.1007/s10915-013-9780-2

- [18] Jameson, A., Vincent, P. E., and Castonguay, P., "On the Non-Linear Stability of Flux Reconstruction Schemes," *Journal of Scientific Computing*, Vol. 50, No. 2, 2012, pp. 434–445.
doi:10.1007/s10915-011-9490-6
- [19] Williams, D., and Jameson, A., "Nodal Points and the Nonlinear Stability of High-Order Methods for Unsteady Flow Problems on Tetrahedral Meshes," *43rd AIAA Fluid Dynamics Conference*, AIAA Paper 2013-2830, 2013.
- [20] Bogey, C., and Bailly, C., "Large Eddy Simulations of Round Free Jets Using Explicit Filtering With/Without Dynamic Smagorinsky Model," *International Journal of Heat and Fluid Flow*, Vol. 27, No. 4, 2006, pp. 603–610.
doi:10.1016/j.ijheatfluidflow.2006.02.008
- [21] Blackburn, H., and Schmidt, S., "Spectral Element Filtering Techniques for Large Eddy Simulation with Dynamic Estimation," *Journal of Computational Physics*, Vol. 186, 2003, pp. 610–629.
doi:10.1016/S0021-9991(03)00088-3
- [22] Karamanos, G., and Karniadakis, G., "A Spectral Vanishing Viscosity Method for Large-Eddy Simulations," *Journal of Computational Physics*, Vol. 163, No. 1, 2000, pp. 22–50.
doi:10.1006/jcph.2000.6552
- [23] Pasquetti, R., "Spectral Vanishing Viscosity Method for LES: Sensitivity to the SVV Control Parameters," *Journal of Turbulence*, Vol. 6, No. 12, 2005, pp. 1–14.
doi:10.1080/14685240500125476
- [24] Grinstein, F., and Fureby, C., "Recent Progress on MILES for High Reynolds Number Flows," *Journal of Fluids Engineering*, Vol. 124, No. 4, 2002, pp. 848–861.
doi:10.1115/1.1516576
- [25] Pasquetti, R., "High-Order LES Modeling of Turbulent Incompressible Flow," *Comptes Rendus Mécanique*, Vol. 333, No. 1, 2005, pp. 39–49.
doi:10.1016/j.crme.2004.09.018
- [26] Galbraith, M., and Visbal, M., "Implicit Large Eddy Simulation of Low Reynolds Number Flow Past the SD7003 Airfoil," *46th Aerospace Science Meeting and Exhibit*, AIAA Paper 2008-0225, 2008.
- [27] Garmann, D., Visbal, M., and Orkwis, P., "Comparative Study of Implicit and Subgrid-Scale Model Large-Eddy Simulation Techniques for Low-Reynolds Number Airfoil Applications," *International Journal for Numerical Methods in Fluids*, Vol. 71, No. 12, April 2013, pp. 1546–1565.
doi:10.1002/flid.3725
- [28] Parsani, M., Ghorbaniasl, G., Lacor, C., and Turkel, E., "An Implicit High-Order Spectral Difference Approach for Large Eddy Simulation," *Journal of Computational Physics*, Vol. 229, No. 14, 2010, pp. 5373–5393.
doi:10.1016/j.jcp.2010.03.038
- [29] Diosady, L., and Murman, S., "Design of a Variational Multiscale Method for Turbulent Compressible Flows," *21st AIAA Computational Fluid Dynamics Conference*, AIAA Paper 2013-2870, June 2013.
- [30] Roe, P. L., "Approximate Riemann Solvers, Parameter Vectors and Difference Schemes," *Journal of Computational Physics*, Vol. 43, No. 2, 1981, pp. 357–372.
doi:10.1016/0021-9991(81)90128-5
- [31] Jameson, A., and Lodato, G., "A Note on the Numerical Dissipation from High-Order Discontinuous Finite Element Schemes," *Computers and Fluids*, Vol. 98, Jan. 2013, pp. 186–195.
doi:10.1016/j.compfluid.2014.01.016
- [32] Allaneau, Y., and Jameson, A., "Connections Between the Filtered Discontinuous Galerkin Method and the Flux Reconstruction Approach to High Order Discretizations," *Computer Methods in Applied Mechanics and Engineering*, Vol. 200, Nos. 49–52, pp. 3628–3636.
doi:10.1016/j.cma.2011.08.019
- [33] Vincent, P. E., Castonguay, P., and Jameson, A., "Insights from von Neumann Analysis of High-Order Flux Reconstruction Schemes," *Journal of Computational Physics*, Vol. 230, No. 22, 2011, pp. 8134–8154.
doi:10.1016/j.jcp.2011.07.013
- [34] Asthana, K., and Jameson, A., "High-Order Flux Reconstruction Schemes with Minimal Dispersion and Dissipation," *Journal of Scientific Computing*, Vol. 62, No. 3, 2015, pp. 913–944.
doi:10.1007/s10915-014-9882-5
- [35] Don, W., Gottlieb, D., and Shu, C., "Numerical Convergence Study of Nearly-Incompressible, Inviscid Taylor–Green Vortex Flow," *Journal of Scientific Computing*, Vol. 24, No. 1, 2005, pp. 1–27.
doi:10.1007/s10915-004-5407-y
- [36] Johnsen, E., Varadan, S., and van Leer, B., "A Three-Dimensional Recovery-Based Discontinuous Galerkin Method for Turbulence Simulations," *51st AIAA Aerospace Sciences Meeting*, AIAA Paper 2013-0515, Jan. 2013.
- [37] Carton de Wiart, C., Hillewaert, K., Duponcheel, M., and Winkelmanns, G. S., "Assessment of a Discontinuous Galerkin Method for the Simulation of Vortical Flows at High Reynolds Number," *International Journal for Numerical Methods in Fluids*, Vol. 74, No. 7, 2014, pp. 469–493.
doi:10.1002/flid.3859
- [38] Bull, J., and Jameson, A., "High-Order Flux Reconstruction Schemes for LES on Tetrahedral Meshes," *Proceedings of the 5th Symposium on Hybrid RANS-LES Methods*, Springer, Switzerland, 2014, pp. 69–79.
- [39] López, M., Sheshadri, A., Bull, J., Economou, T., Romero, J., Watkins, J., Williams, D., Palacios, F., Jameson, A., and Manosalvas, D., "Verification and Validation of HiFiLES: A High-Order Navier–Stokes Unstructured Solver on Multi-GPU Platforms," *44th AIAA Fluid Dynamics Conference*, AIAA Paper 2014-3168, June 2014.
- [40] Rusanov, V. V., "Calculation of Interaction of Non-Steady Shock Waves with Obstacles," *USSR Computational Mathematics and Mathematical Physics*, Vol. 1, No. 2, 1962, pp. 304–320.
- [41] Kannan, R., and Wang, Z., "LDG2: A Variant of the LDG Flux Formulation for the Spectral Volume Method," *Journal of Scientific Computing*, Vol. 46, No. 2, 2011, pp. 314–328.
doi:10.1007/s10915-010-9391-0
- [42] Jameson, A., "A Proof of the Stability of the Spectral Difference Method for all Orders of Accuracy," *Journal of Scientific Computing*, Vol. 45, No. 1, 2010, pp. 348–358.
doi:10.1007/s10915-009-9339-4
- [43] Fischer, P., and Mullen, J., "Filter-Based Stabilization of Spectral Element Methods," *Comptes Rendus de l'Académie des Sciences, Series I: Mathematics*, Vol. 332, No. 3, 2001, pp. 265–270.
doi:10.1016/S0764-4442(00)01763-8
- [44] Castonguay, P., Liang, C., and Jameson, A., "Simulation of Transitional Flow over Airfoils Using the Spectral Difference Method," *AIAA Fluid Dynamics Conference and Exhibit*, AIAA Paper 2010-4626, June–July 2010.
- [45] Ou, K., and Jameson, A., "Towards Computational Flapping Wing Aerodynamics of Realistic Configurations Using Spectral Difference Method," *20th AIAA Computational Fluid Dynamics Conference*, AIAA Paper 2011-3068, 2011.
- [46] Ou, K., Castonguay, P., and Jameson, A., "3-D Flapping Wing Simulation with High Order Spectral Difference Method on Deformable Mesh," *49th AIAA Aerospace Sciences Meeting*, AIAA Paper 2011-1316, 2011.
- [47] Lodato, G., Castonguay, P., and Jameson, A., "Discrete Filter Operators for Large-Eddy Simulation Using High-Order Spectral Difference Methods," *International Journal for Numerical Methods in Fluids*, Vol. 72, No. 2, 2012, pp. 231–258.
doi:10.1002/flid.3740
- [48] Debonis, J., "Solutions of the Taylor–Green Vortex Problem Using High-Resolution Explicit Finite Difference Methods," *51st AIAA Aerospace Sciences Meeting*, AIAA Paper 2013-0382, Jan. 2013.
- [49] Bogey, C., and Bailly, C., "A Family of Low Dispersive and Low Dissipative Explicit Schemes for Flow and Noise Computations," *Journal of Computational Physics*, Vol. 194, No. 1, 2004, pp. 194–214.
doi:10.1016/j.jcp.2003.09.003
- [50] Persson, P., and Peraire, J., "Sub-Cell Shock Capturing for Discontinuous Galerkin Methods," *44th AIAA Aerospace Sciences Meeting and Exhibit*, AIAA Paper 2006-0112, Jan. 2006.
- [51] Sheshadri, A., and Jameson, A., "Shock Detection and Capturing Methods for High Order Discontinuous-Galerkin Finite Element Methods," AIAA Paper 2014-2688, 2014.
- [52] Colonius, T., and Lele, S. K., "Computational Aeroacoustics: Progress on Nonlinear Problems of Sound Generation," *Progress in Aerospace Sciences*, Vol. 40, No. 6, 2004, pp. 345–416.
doi:10.1016/j.paerosci.2004.09.001